



# Synchrotron radiation-based materials characterization techniques shed light on molten salt reactor alloys

Li Jiang<sup>1</sup> · Xiang-Xi Ye<sup>1</sup> · De-Jun Wang<sup>2</sup> · Zhi-Jun Li<sup>1</sup>

Received: 27 July 2019/Revised: 18 October 2019/Accepted: 9 November 2019/Published online: 26 December 2019  
© China Science Publishing & Media Ltd. (Science Press), Shanghai Institute of Applied Physics, the Chinese Academy of Sciences, Chinese Nuclear Society and Springer Nature Singapore Pte Ltd. 2019

**Abstract** From a safety point of view, it is important to study the damages and reliability of molten salt reactor structural alloy materials, which are subjected to extreme environments due to neutron irradiation, molten salt corrosion, fission product attacks, thermal stress, and even combinations of these. In the past few years, synchrotron radiation-based materials characterization techniques have proven to be effective in revealing the microstructural evolution and failure mechanisms of the alloys under surrogating operation conditions. Here, we review the recent progress in the investigations of molten salt corrosion, tellurium (Te) corrosion, and alloy design. The valence states and distribution of chromium (Cr) atoms, and the diffusion and local atomic structure of Te atoms near the surface of corroded alloys have been investigated using synchrotron radiation techniques, which considerably deepen the understandings on the molten salt and Te

corrosion behaviors. Furthermore, the structure and size distribution of the second phases in the alloys have been obtained, which are helpful for the future development of new alloy materials.

**Keywords** Molten salt reactor · Alloy materials · Synchrotron radiation · Shanghai Synchrotron Radiation Facility · Molten salt corrosion · Tellurium corrosion

## 1 Introduction

A molten salt reactor (MSR), which was first proposed in the 1950s, is a series of nuclear reactors in which fluoride or chloride salts are used as coolants and fuels [1]. The MSR concept was initially implemented in an aircraft reactor experiment (ARE) to offer a pony-size nuclear engine for an aircraft nuclear propulsion (ANP) program and then in the molten salt reactor experiment (MSRE) by the Oak Ridge National Laboratory (ORNL) as a civilian nuclear power source [2]. MSRs have many apparent advantages and unique applications, such as the utilization of thorium fuel, small modular designs, and high-temperature hydrogen production. In the past decade, MSRs have received increased attention owing to their advantages over conventional reactors [3]. In 2011, the Chinese Academy of Sciences (CAS) launched the strategic pioneering science and technology project of thorium molten salt reactor nuclear energy systems (TMSR) [4]. Led by the Shanghai Institute of Applied Physics (SINAP), the TMSR project will result in a 2 MW experimental reactor before 2020 [4].

The reliability and robustness of the structural materials, which will suffer from harsh service environments, including high temperatures, molten salt corrosion, and

---

This work was supported by the National key research and development program of China (Nos. 2016YFB0700401 and 2016YFB0700404), Natural Science Foundation of Shanghai (Nos. 19ZR1468200 and 18ZR1448000), National Natural Science Foundation of China (Nos. 51671154, 51601213 and 51671122), Strategic Priority Research Program of the Chinese Academy of Sciences (No. XDA02004210), and Youth Innovation Promotion Association, Chinese Academy of Science (No. 2019264).

---

✉ De-Jun Wang  
wang.dejun@mee.gov.cn

✉ Zhi-Jun Li  
lizhijun@sinap.ac.cn

<sup>1</sup> Shanghai Institute of Applied Physics, Chinese Academy of Sciences, Shanghai 201800, China

<sup>2</sup> Ministry of Ecology and Environment, Beijing 100135, China

high irradiation doses, are considered to be the most significant challenges in the development of MSRs. An eligible Ni-Mo-Cr-based superalloy (Hastelloy N or INOR-8 alloy) was developed in the ORNL during the 1950s and 1960s and exhibited high-temperature strength and excellent corrosion resistance to molten fluoride salts [5]. A few flaws (helium embrittlement and Te embrittlement) were found after its service in the MSRE from 1965 to 1969, which further motivated the research activities on the Ti-modified and Nb-modified versions in the 1970s [6, 7]. During the development of Hastelloy N and its modified versions, a large amount of research data and many composition–structure–performance relationships were reported by the ORNL. The most important ones were related to molten salt corrosion, Te corrosion, and the roles of key constituents. Unfortunately, the detailed mechanisms of these interesting relationships were not revealed owing to the lack of suitable characterization techniques and theoretical tools at that time.

Since the last century, synchrotron radiation theory and the related facilities have developed rapidly. Their apparent advantages over conventional characterization tools include high brilliance, wide energy spectrum, very short pulses, good collimation of emitted radiation, and source cleanliness. Synchrotron radiation techniques have been widely applied in the study of superalloys. Benchmark results include the (1) measurement of the lattice misfit by high-energy synchrotron radiation diffraction [8]; (2) determination of local strains and microstructure by synchrotron radiation scanning Laue X-ray microdiffraction [9, 10]; (3) synchrotron tomography of porosity and crack [11, 12]; (4) evaluation of residual stresses [13], and (5) the determination of environment interactions [14]. Synchrotron radiation is expected to solve the remaining problems with alloy materials in MSRs. For example, there were some difficulties in the phase identification of different tellurides on the alloy surface using conventional x-ray diffraction techniques. The interference from other unknown impurity phases and the tiny difference between the different nickel tellurides ( $\text{NiTe}_{0.67}$ ,  $\text{NiTe}_{0.69}$ ,  $\text{NiTe}_{0.70}$ ,  $\text{NiTe}_{0.77}$ , and  $\text{NiTe}_2$ ) made the precise phase identification impossible. This could be solved by synchrotron radiation X-ray diffraction owing to its higher brilliance. Synchrotron radiation-based material characterization techniques can also be expected to deepen the understanding of the related mechanisms in the MSR alloys, which is required for the further optimization of this alloy or the design of new ones (Table 1).

In 2004, the SINAP started building the Shanghai Synchrotron Radiation Facility (SSRF), which was fully opened to users in 2009 [15]. When the TMSR team was organized in 2011, many scientists from the SSRF came in and dealt with the problems mentioned above using

synchrotron radiation technology. In this article, we will review the related works to demonstrate the new understanding of the microstructural evolutions and failure behaviors of alloy materials for MSRs and clarify the availability of synchrotron radiation applications in this field. The new progress is introduced in three sections: (1) molten salt corrosion, (2) Te corrosion, and (3) alloy design. Today, most of the related studies are carried out in the SSRF. Thus, we give a brief introduction of the beamlines in the SSRF used in these studies. In addition, the more promising applications of synchrotron radiation in this field are discussed.

## 2 Materials and Methods

### 2.1 Development of Alloy Materials for MSRs

During the ANP period, the ORNL was responsible for both the design and building of the ARE, which involved the synchronous screening of fuel, coolant, and alloy materials. In 1950, the fluoride 75% NaF-25%  $\text{UF}_4$  was firstly proposed as the fuel candidate [16]. Then, the important criterion for the screening of structural materials was the chemical compatibility with molten fluoride salts. In the dynamic corrosive conditions of thermal convection loops, the Inconel 600 alloy operated well [17]. In 1954, the ARE produced 100 MWh over nine days at a peak temperature of 860 °C with the Inconel 600 alloy as the structural material. However, the Inconel 600 alloy can hardly meet the high-temperature strength and corrosion resistance requirements of the MSRE. The ORNL started developing a new alloy based on the Ni-Mo binary system. It was found that the addition of Mo of less than 15 wt. % produces insufficient high-temperature strength. However, the Mo content was preliminarily limited to 20 wt. % in consideration of the pipe extrusion processability and thermal stability. In the range of 15–20 wt. % Mo, further addition of Mo can lead to better creep properties in the Ni-Mo-Cr-Fe alloys. In view of the unavoidable exposure to hot air, the addition of Cr is necessary for the oxidation resistance of alloys. However, it has been revealed that Cr would be removed from the hotter parts of the loop and deposited in the cooler parts when reacting with  $\text{UF}_4$  (more details in Sect. 3). Thus, the Cr content should be as low as possible to obtain the lowest corrosion rate in fluoride salts. Cr contents of 6–8 wt. % can prevent the oxidation from air at 700 °C, but are not enough to induce high molten salt corrosion rates. At the time of the ARE, Cr was always added in the form of cheap Fe-Cr alloys rather than in the expensive elemental state. The presence of minor amounts of Fe (< 6 wt. %) does not drastically affect the properties of alloys. Based on the above results, several promising

**Table 1** Chemical compositions of alloys for MSRs

	N INOR-8	Ti-modified N	Nb-modified N	HN80MTY	MONICR	GH3535	EM-721
Ni	Bal.	Bal.	Bal.	Bal.	Bal.	Bal.	Bal.
Mo	16	12.97	11.71	13.2	15.8	16	0.07
Cr	7	6.97	6.78	6.81	6.85	7	5.7
Fe	5	0.08		0.15	2.27	4	0.05
Mn	0.8	0.02	0.1	0.013	0.037	0.5	0.086
Si	1	0.03		0.04	0.13	0.3	0.065
Ti		1.8		0.93	0.026		0.13
Nb			1.15	0.01			
Al		0.1		1.12	0.02		0.08
W	0.5	0.01		0.072	0.16		25.2
C	0.08	0.06	0.043	0.025	0.014	0.05	

nickel-based alloys, codenamed INOR-1 to INOR-9, were melted and evaluated, and INOR-8 (Table 1) was found to meet all requirements [18].

The ANP program was discontinued in 1960, and the mission of the program was shifted to the MSRE program. In this period, long-term corrosion experiments and the evaluation of the mechanical properties were carried out on several heats purchased from different manufacturers to ensure that the properties were equivalent to those measured from the laboratory-level INOR-8. An alloy with a composition very close to that of INOR-8 was then commercialized by Haynes as Hastelloy N and played a crucial role in the success of the MSRE. However, examinations of the alloy materials after the shutdown of the MSRE revealed two serious deficiencies. First, the alloy was embrittled by helium due to the transmutation of tramp  $^{10}\text{B}$  [19]. Second, the Te fission products in all alloy materials in contact with the fuel salts resulted in surface intergranular cracking [20]. The critical helium concentration required to embrittle the alloy is so low that reducing the boron concentration is not effective [21]. An effective solution for the helium embrittlement problem is to add IVB and VB group elements (typically Ti) into Hastelloy N; these preferentially form fine MC carbides to trap the helium atoms at their interface with the matrix and prevent the growth of helium bubbles at grain boundaries [22]. The ORNL researchers proceeded with the development of Ti-modified Hastelloy N. At a later time, they observed that the addition of 1 to 2 wt. % of Nb to Hastelloy N could effectively prevent helium and Te embrittlement synchronously.

In the new century, the MSR concept has attracted more attention owing to the advantages mentioned above. Thus, the development of structural materials for MSRs has again become an important topic. Based on Hastelloy N, improved versions have been proposed, including the Fe-reduced MONICR alloy [23] and Al-modified HM80M

series [24], which exhibit better creep properties and Te corrosion resistance, respectively. In France, a new Ni-W-Cr-based superalloy (EM-721) was developed, which can endure potentially higher in-service temperatures [25]. The ORNL is developing some new nickel-based alloys with high-temperature strength higher than that of Hastelloy N for use in fluoride salt-cooled high-temperature reactors (FHRs) [26]. Based on Hastelloy N, the GH3535 alloy has been developed for TMSRs [7], and its composition optimization (Si and C), extensive characterization, and the process development of large-scale components are being carried out. The related synchrotron radiation technique-assisted studies are reviewed in this paper.

## 2.2 Shanghai Synchrotron Radiation Facility (SSRF)

For the SSRF Phase-I program, seven beamlines have been built, namely the macromolecular crystallography (BL17U1) [27, 28], X-ray absorption fine structure (XAFS, BL14W1) [29], diffraction (BL14B1) [30], hard X-ray micro-focusing (BL15U1) [31], X-ray imaging (BL13W1) [32], soft X-ray spectromicroscopy (BL08U1A) [33, 34], and small-angle X-ray scattering (SAXS, BL16B1) beamlines [35]. In this article, we review the studies related to BL14W1, BL15U1, BL08U1A, and BL16B1.

The XAFS beamline (BL14W1) at the SSRF is a powerful platform to explore the local structure of materials [29]. At present, standard XAFS data can be collected in transmission and fluorescence yield modes. In addition, the quick-scanning XAFS (QXFAS), X-ray emission spectroscopy (XES), grazing incidence XAFS (GIXAFS), high-pressure XAFS, and time-resolved X-ray excited optical luminescence methods will gradually become available to users in the future.

The hard X-ray micro-focusing beamline (BL15U1) of the SSRF is mainly aimed at hard X-ray micro/nano-

spectrochemical analyses, including micro-beam X-ray fluorescence ( $\mu$ -XRF), X-ray absorption spectroscopy (XAS), and synchrotron radiation X-ray diffraction (SR-XRD) [31]. The BL15U1 beamline provides high-brightness X-rays with energy ranging from 4.9 to 20.5 keV. It is also capable of micro-focusing as low as  $\sim 2 \mu\text{m}$ . The beamline and the experimental end station were upgraded several times to facilitate the users' experimental needs and make it more convenient to operate. In the BL15U1 beamline, a motorized  $x-y-z$  stage with a high step precision of 100 nm allows hyperfine scanning in the beam for XRF, XRD, and XAS (Fig. 1). With this stage, the phase distribution, composition distribution, and valence state information of an element can be obtained simultaneously by XRF mode scanning and XRD mode scanning of the same region.

The BL08U1A beamline is a soft X-ray beamline with a photon beam energy range of 250 to 2000 eV and is aimed at nanoscale elemental imaging at high spatial and energy resolutions [33, 34]. 2D and 3D imaging of metallic materials can be performed in the scanning transmission X-ray microscopy (STXM) end station. The STXM combines high spatial and energy resolutions of the chemical states of near-edge absorption fine structure spectroscopy (XANES). The scanning precision of piezo-stages is approximately 5 nm, and the scanning range can be selected from several microns to several hundred microns. Coherent diffraction imaging (CDI) can offer higher spatial resolution than STXM, which is also installed at the STXM chamber (Fig. 2). The highest resolution of CDI is approximately 10 nm, derived from a power spectral density analysis of the reconstructed image using scanning CDI reconstruction software.

The SAXS beamline (BL16B1) at the SSRF provides a powerful support for studying the microstructure of polymers, fibers, and nanostructure/mesoporous materials [35]. The techniques available in the beamline include SAXS,

wide-angle X-ray scattering (WAXS), anomalous small-angle X-ray scattering (ASAXS), grazing incident SAXS (GISAXS), and time-resolved simultaneous SAXS/WAXS on structural transitions in the sub-second time region and partly ordered systems with a scaling of 1 to 240 nm in real space. More techniques will be implemented at the BL16B1, including the USAXS technique based on the Bonse–Hart camera system and micro-focus SAXS. Additional common in situ devices to facilitate the use of this beamline will be developed. A complete SAXS data analysis platform will be established for data pretreatment, SAXS and WAXS data analyses, etc.

### 3 Molten Salt Corrosion

In most high-temperature environments, the desired corrosion resistance of materials is achieved by the formation of a compact and protective oxide film on the alloy surface. For high-temperature applications in oxygen-containing environments, alloy elements, such as Cr and Al, are commonly used to facilitate the formation of protective oxide films to retard further oxidation. However, in fluoride salt systems, any such protective oxide scales are not stable and can be easily dissolved by the fluxing action of molten fluoride salts and, thus, cannot be relied upon for corrosion protection. The corrosion of alloys in molten salts has been extensively studied [14, 37–43] and reviewed [44–48], since the foundational work for the use of molten salts in nuclear energy applications was performed at the ORNL from the 1940s to the 1970s. Briefly, the molten salt corrosion of alloys is driven by a variety of factors, including the thermodynamics of corrosion reactions [42, 43], impurity effects [14, 40, 41], thermal gradients [49, 50], and galvanic corrosion induced by the difference of electromotive potential in materials [51, 52].

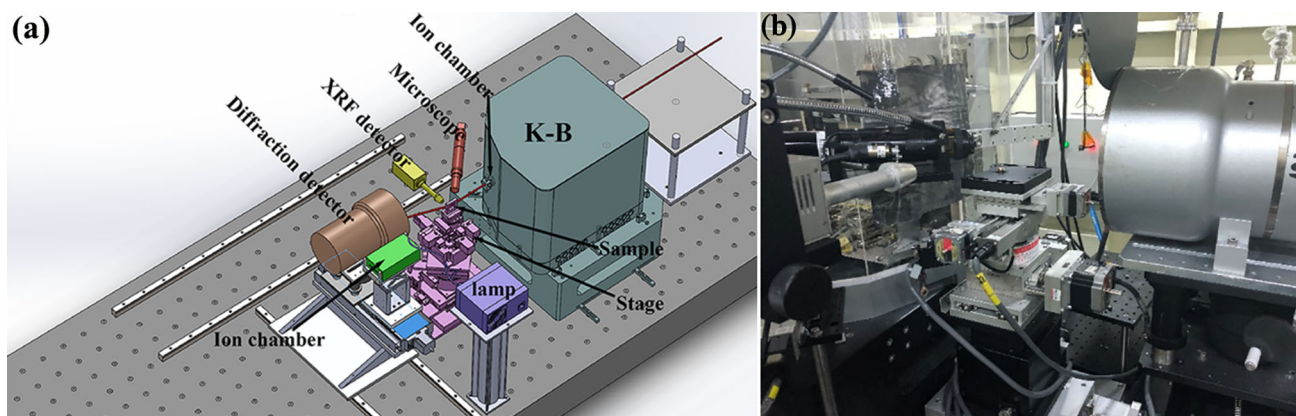


**Fig. 1** (Color online) (a) Schematic and (b) photograph of the integrated XRF, XRD, and XAS equipment at the BL15U1 beamline (reprinted from [36])

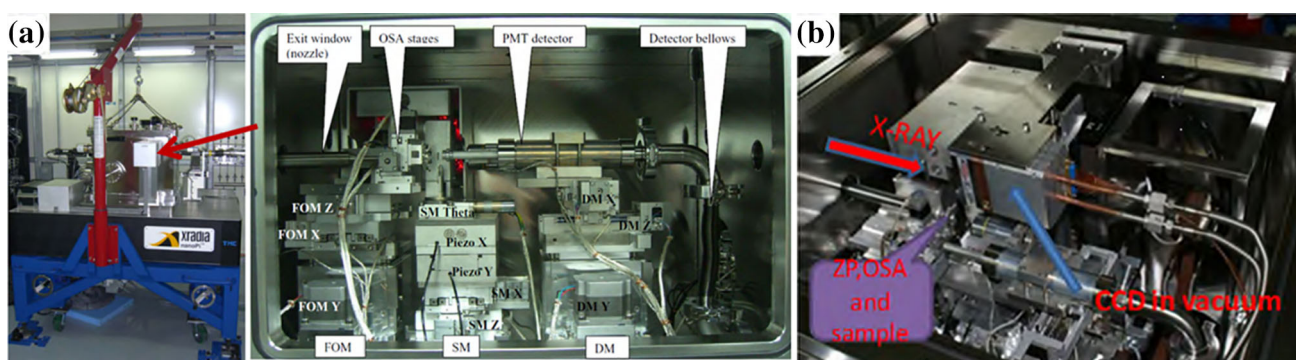


**Fig. 2** (Color online) (a) STXM chamber and its inner components, including (b) a CDI experiment platform (reprinted from [33])

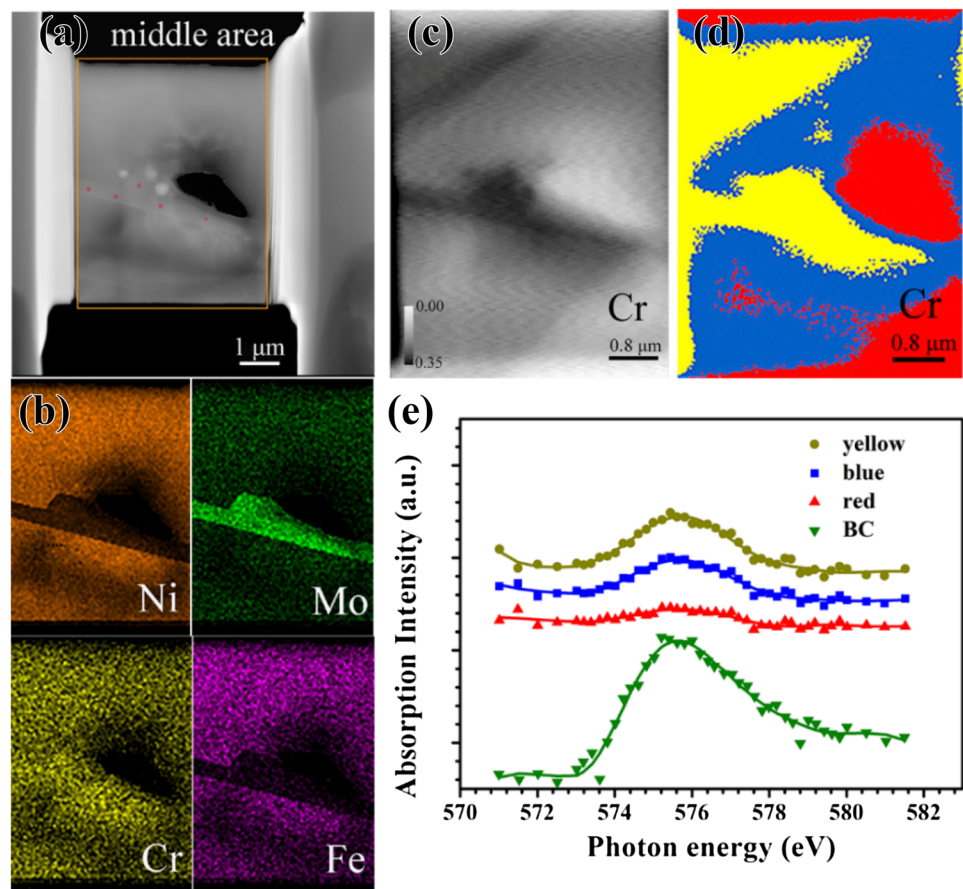
During the corrosion process of alloys in molten salt, the elements that form fluorides with more negative free Gibbs energies would preferentially react with molten salt and transfer from the alloy into the molten salt. The list of fluoride-forming elements used in Ni-based and Fe-based alloys is, from the least to the most thermodynamically favorable, as follows: Al, Cr, Fe, Ni, Mo, and W. In view of the greater stability of molten fluoride salts (LiF, BeF<sub>2</sub>, NaF, KF, etc.) over that of potential corrosion products, the corrosion of these elements should, in theory, not occur. However, the unavoidable impurities in the molten salts, including H<sub>2</sub>O, HF, and metallic ions (Ni<sup>2+</sup>, Fe<sup>2+</sup>), would react with the alloys by redox reactions and cause considerable corrosion, as reported in [41].

Techniques based on synchrotron radiation, such as XRF, XANES, and STXM, are powerful for measuring the elemental concentration and chemical state of reaction products at micro- and nanoscale, which can reveal the type of chemical reaction and the corrosion mechanism. However, to date, few studies on these methods have been reported in the literature. Liu et al. [53] were the first to apply  $\mu$ -XRF and SR-XRD techniques at the SSRF to evaluate the corrosion behavior of different Ni-based alloys. The  $\mu$ -XRF mapping from the cross section shows the poor corrosion resistance of all the alloys to molten salts, and that the alloys are significantly depleted in Cr. Interestingly, Mo<sub>2</sub>C was detected by SR-XRD, a result of the galvanic reaction between the alloys and the graphite crucibles. This phenomenon can also occur in real molten salts reactors because they use graphite as a neutron moderator. In addition, small amounts of Cr<sub>2</sub>O<sub>3</sub>, which should not be stable in molten salts, were also found to form in the corroded Inconel 600 and Hastelloy C-276 alloys, indicating the high content of oxygen impurities in the FLiNaK salts. It should be noted that such a small amount of Mo<sub>2</sub>C or Cr<sub>2</sub>O<sub>3</sub> is difficult to detect in laboratory XRD.

Another study on the corrosion behavior of nickel alloys based on synchrotron radiation techniques was reported by

Ye et al. [14]. As mentioned above, the presence of oxidizing impurities greatly facilitates the corrosion of alloys in the molten salts. Among the impurities, the role of H<sub>2</sub>O in the corrosion process has been determined. HF can form during the reaction between H<sub>2</sub>O and the fluoride ions and would attack most metal elements in the alloys to form the corresponding fluorides. So far, the concentration of H<sub>2</sub>O in the fluoride salts can be controlled to a level of less than 10 ppm by several methods [43, 54, 55]. In contrast, studies on the role of other metallic ion impurities (e.g., Fe<sup>+2</sup>, Fe<sup>+3</sup>, Cr<sup>+2</sup>, Cr<sup>+3</sup>, and Ni<sup>+2</sup>) in the corrosion process are still limited. In other words, besides the redox reaction, it is not clear whether some other types of reaction, as well as composition changes in the precipitates, may occur in the alloys. Ye et al. applied STXM and XANES with the assistance of the stage with high positional accuracy (Fig. 1) to characterize the corroded and control Hastelloy N alloys at the BL15U1 beamline. The XANES results showed that no oxidized compound of Fe formed in the corroded specimen, indicating that only a redox reaction, e.g., Cr + Fe<sup>2+</sup> = Cr<sup>2+</sup> + Fe, occurs in the alloys surface, causing depletion of Cr in the alloys. This result suggests that only the redox reaction can occur during the molten salt corrosion (Fig. 3e). In addition, a different Cr concentration in the M<sub>12</sub>C carbides and matrix after corrosion was detected by STXM, indicating that Cr diffused from M<sub>12</sub>C carbides to the matrix, which could not be measured clearly by TEM/EDS. As shown in Fig. 3d and e, the depletion and enrichment of Cr can be observed before and after the corrosion process, respectively. The steep concentration gradient of Cr in the matrix, which results from the redox reaction, would further drive the diffusion of Cr atoms from the carbide into the matrix. This may be the first work based on SR-STXM method to investigate the properties of Ni-based alloys. The results obtained in nanoscale by STXM and XANES are useful for our understanding of the effect of metallic impurities (e.g., Fe<sup>+2</sup>, Fe<sup>+3</sup>, Cr<sup>+2</sup>, Cr<sup>+3</sup>, and Ni<sup>+2</sup>) on the corrosion of alloys in FLiNaK salts.

**Fig. 3** (Color online) (a) TEM images of the region 5 ~ 9  $\mu\text{m}$  distance away from the surface; (b) TEM/EDS maps of rectangle area in panel (a); (c) STXM transmission images of Cr at 572 eV; (d) color-coded maps of Cr, derived from an STXM Cr L-edge stack analysis; and (e) XANES extracted from the image of Cr (c) ( adapted from [14])



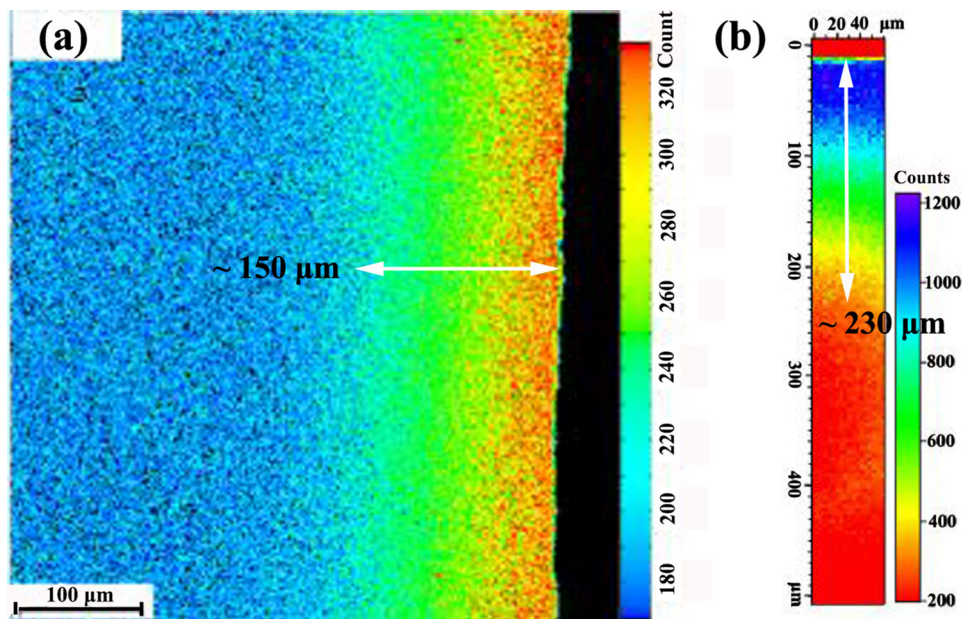
## 4 Te Corrosion

### 4.1 Te Distribution by SR-XRF

As mentioned above, Te atoms diffuse along the surface grain boundaries and then cause the intergranular cracking of alloys. In general, the diffusion mode (grain boundary or lattice) of impurities in metals transforms in the moderate temperature range. Thus, it is necessary to investigate the diffusion of Te atoms in pure nickel and the reaction between them in the moderate temperature range (500–1000 °C) to understand the Te embrittlement in the GH3535 alloy. In such an investigation, the characterization method used to determine the Te distribution is the most important aspect. XRF spectroscopy is a powerful nondestructive method for the analysis of trace elements in material science research, and BL15U1 enables XRF multi-element mapping and quantitative analysis with a sub-ppm level detection limit and a micro- or sub-microlevel beam size [31]. Thus, the cross-sectional micro-XRF maps of Te in the samples, which are exposed to Te vapor at 500–1000 °C, were examined with a monochromatic 5 keV X-ray beam in BL15U1 [56]. For comparison, electron probe microanalysis (EPMA) examinations were

also carried out. The typical results for the samples exposed at 1000 °C are shown in Fig. 4. SR-XRF revealed a higher Te diffusion depth than EPMA, which indicates the higher sensitivity to Te atoms in the SR-XRF detection. The critical value of the Te concentration for intergranular cracking can be very low, but the precise measurement of the Te distribution is necessary. It has been reported [57] that the diffusion depth of Te was significantly underestimated by the EPMA measurements and was smaller than that of intergranular fractures observed from the tensile specimens. This indicated that the critical damage level of Te for GH3535 alloy is lower than the EMPA detection limit. From Fig. 4, it can be seen that the diffusion depth measured by SR-XRF can reflect the damage behaviors by Te corrosion more accurately than EPMA. Unfortunately, the low lateral resolution of SR-XRF detection in this study cannot reveal the enrichment of Te at grain boundaries effectively. A nano-focusing (100 nm) fluorescence system has been built on BL15U1, and improvements to the flux and efficiency of detection are underway [31].

**Fig. 4** (Color online) (a) EPMA mapping and (b) SR-XRF mapping for the samples exposed to Te vapor at 1000 °C ( adapted from [56])



## 4.2 Local Structure of Te atoms in alloys

Despite the predominant role of Te corrosion at the grain boundaries, its diffusion and enrichment in the lattice can also influence the microstructures and mechanical properties of GH3535 alloy. The occupied sites of Te atoms in the FCC matrix and their effects on the lattice are still unclear. Limited experiment results have indicated that the lattice of the matrix expands after Te corrosion. Thus, the local structure of Te atoms in the corrosion products or the matrix lattice was investigated by extended XAFS (EXAFS) and first-principles calculations [58]. As shown in Fig. 5, the radial distribution functions (RDFs) of the corroded and control specimens of pure Ni and Te were

extracted from their  $k^2$ -weighted EXAFS. The absence of a prominent peak at 2.6 Å for Te in the RDF indicates that Te clusters did not exist in the Te-exposed sample, and the similarity of the local structure around Te atoms between corroded and Ni samples proves that Te atoms randomly solubilize in FCC Ni to form the substitutional solid solution. Provided Te atoms are surrounded by Ni atoms in the FCC Ni; the fitting curve of the EXAFS signal in R-space with the contribution from each of the three nearest neighbor shells agrees well with the experimental curve. Moreover, the bond length for the nearest three shells is larger than that predicted with theoretical data of pure Ni. EXAFS proved that the lattice expansion of the corroded Ni results from the substitution of Te. This

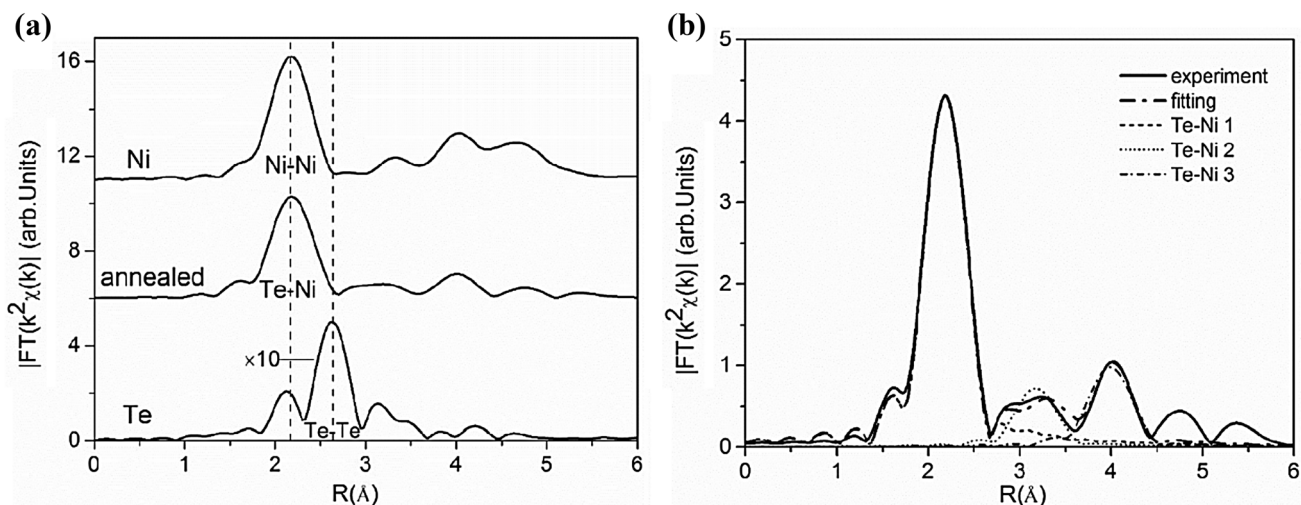


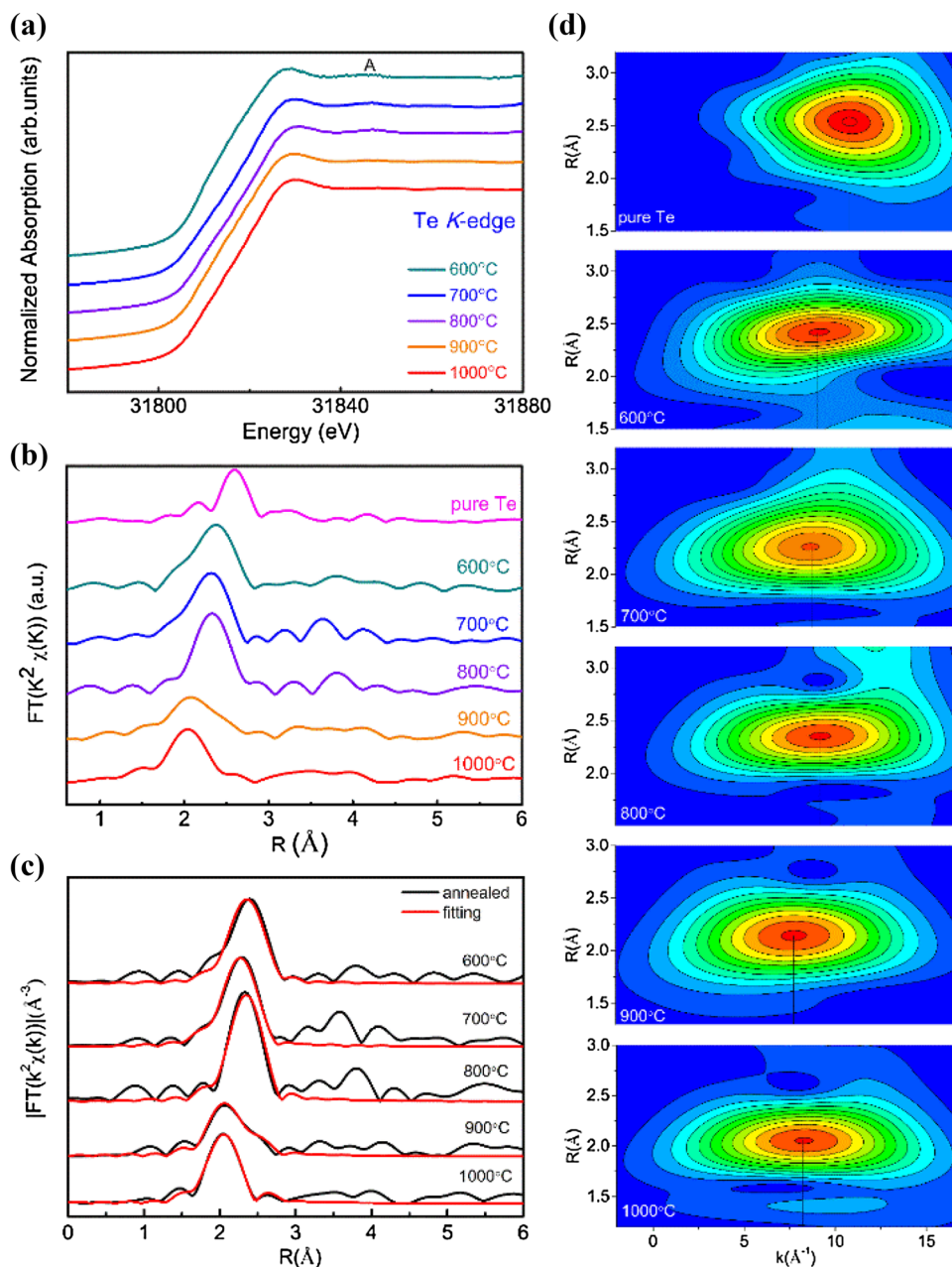
**Fig. 5** (a) RDF and (b) typical fitting curve of the EXAFS signal in R-space for the corroded specimens and the contributions from each shell (reprinted from [58])

conclusion can also be verified by DFT calculations. In the case of the nearest neighbor Te–Te pair, the negative energy value indicates that such a configuration is energetically unfavorable in the Ni substrate.

To overcome the Te corrosion problems, researchers are trying to optimize the chemical composition and microstructure of alloys. It is worth noting that high-chromium alloys always exhibit higher Te corrosion resistance. Using XANES, one Ni-18Cr alloy was corroded by Te vapor at different temperatures (600–1000 °C), and the local structure of Te atoms in the corroded samples was determined [59]. Figure 6 displays the XANES results of the Te K-edge. From the peak positions in the Fourier

transform (FT) curves of these samples, the Cr–Te scattering contribution can be observed, which indicates the existence of chromium telluride as a corrosion product. In the case of the specimens corroded at 900 °C, a much lower R position indicates the dominance of the Ni–Te contributions, which correspond to the formation of partial Ni<sub>3</sub>Te<sub>2</sub>. Using wavelet transform (WT) analysis, the corrosion product was determined to be a substitutional Ni–Cr–Te solid solution in the specimens corroded at 1000 °C. The XANES has proved to be a powerful tool for exploring the structure and composition of corrosion products, which can deepen our understanding of the protection mechanism of certain tellurides.

**Fig. 6** (Color online) (a) X-ray absorption spectra at the Te K-edge; (b) RDFs and (c) typical fitting curves of the Te EXAFS signal in R-space for five species annealed between 600 and 1000 °C. (d) Wavelet transforms for the k<sup>2</sup>-weighted Te K-edge EXAFS signals for the high-coordination shells (adapted from [59])





## 5 Alloy Design

### 5.1 Lattice parameter measurement of minor $M_6C$ carbides by HESXRD

Si is always used in small amounts as a deoxidizer during the melting of nickel-based superalloys. With a few exceptions, as noted below, its presence in Hastelloy N has significant effects on the microstructures and properties of this alloy [60], which indicates a large potential for the optimization of Si concentration. To systematically determine the role of Si, the morphology, microstructure, composition, and phase transformation of the carbides in the GH3535 alloys were investigated, with different Si concentrations, in the cast state, solid-solution state, and thermal exposure state, respectively. It was found that Si addition stabilizes  $M_6C$  carbides at high temperatures in GH3535 alloys [61].

$M_6C$  carbides, which belong to the space group  $Fd3m$  and have three forms ( $A_3B_3C$ ,  $A_4B_2C$ , and  $A_2B_4C$ ), are characterized by chemical and structural flexibility [62]. No general agreement, about the atomic occupancy of Si (A, B, or C) in  $M_6C$  carbides in other alloys, has been reached by conventional characterization techniques [63–65]. The interaction of Si atoms with the neighboring atoms in  $M_6C$  carbides was also not clear until the combined utilization of the synchrotron radiation techniques and first-principles calculations [61]. Assuming one Si atom occupies four different sites (16d, 32e, 48f, and 16c) in the  $Ni_3Mo_3C$  system, the equilibrium lattice parameters and site occupancy energies were calculated and compared with those of the initial  $Ni_3Mo_3C$  without Si doping. The equilibrium lattice was found to shrink when the 16d, 32e, and 48f sites were occupied, but it was found to expand when Si atoms replaced C atoms at the 16c site. The actual lattice parameters should be examined to validate these results. In other studies, carbides for XRD were always anodically extracted with a cathode in a mixed solution, typically 25% HCl-75% methanol. However, this technique is not suitable for our small sample ( $10 \times 10 \times 1 \text{ mm}^3$ ). In the sample with 0.05 wt. % Si, the  $M_6C$  carbides extracted for XRD were largely insufficient. However, the alloying effects of a small number of Si additions in  $M_6C$  carbides could be out of the detection limit of laboratory XRD. Thus, high-energy synchrotron X-ray diffraction (HESXRD) was applied to examine the lattice parameters of the  $M_6C$  carbides in the matrix without extraction. In the HESXRD experiment, the high brilliance and good collimation can ensure a relative error as low as  $\sim 2 \times 10^{-4}$  for the lattice spacing. From Fig. 7, it can be seen that the lattice parameters of  $M_6C$  carbides decrease with increasing Si concentrations, and the decrease rate becomes

smaller with increasing Si concentrations, which is slightly different from the linear decrease trends observed in other alloys by laboratory XRD equipment [66]. In  $M_6C$  carbides, Si is just a doped element rather than a required component. It seems reasonable that there exists a saturated content for the doped Si atoms and then a saturated effect of lattice shrinking, as shown in Fig. 7c. Such a saturation effect can also be observed in the formation energy vs Si content curve for the Si-doped  $Ni_3Mo_3C$  system obtained by first-principles calculations. In that study, HESXRD could reveal the tiny but interesting details about the alloying effects of Si, which had not been reported previously. By combining the calculation results and HESXRD data, it can be deduced that the 16d site, rather than other sites, is preferentially occupied by Si atoms in the  $Ni_3Mo_3C$  carbides.

### 5.2 Optimization of W content in Ni-xW-6Cr alloy by $\mu$ -XRF, $\mu$ -XRD, and $\mu$ -XANES

The Ni-W-Cr-based superalloy has been considered a potential candidate structural material for molten salt reactors operating above 800 °C, which is designed to use W as a solid-solution strengthening element, replacing the counterpart Mo in Hastelloy N [25]. Preliminary studies indicate that the strength increases significantly with increasing W concentration in the Ni-xW-6Cr alloys [67]. In addition, the Ni-26 W-6Cr alloy exhibits a corrosion resistance comparable to that of GH3535 alloy [68, 69]. Because the alloy materials in MSR are exposed to air and molten salts simultaneously, the oxidation behavior of the alloys should be considered. Unfortunately, the role of W in the oxidation process of superalloys is still unclear [70–73]. In Hastelloy N, 6–8 wt. % Cr additions are just enough to achieve an oxidation resistance of up to 750 °C. Thus, the oxidation resistance of the Ni-xW-6Cr alloys is questionable.

In a recent work [36], the oxidation resistance of the Ni-xW-6Cr ( $X = 5\text{--}30$ ) alloys at high temperature was investigated. The resistance was found to increase with the W concentration, although not steadily, and the Ni-25 W-6Cr alloy exhibited the best resistance. The phase constituent and chemical state of oxide scales were characterized by  $\mu$ -XRF, micro-XRD ( $\mu$ -XRD), and micro-XANES ( $\mu$ -XANES) at BL15U1. The distribution of oxides and related oxidation reactions in the Ni-xW-6Cr alloys are illustrated in Fig. 8 and were identified by  $\mu$ -XRF and  $\mu$ -XRD at 20 keV. As a secondary acceptor of the inward diffused oxygen, the presence of W facilitates the formation of  $Cr_2O_3$  and  $NiCr_2O_4$  in the regions with lower concentrations of Cr (Fig. 9). In sequence, the increase in the W concentration in the Ni-xW-6Cr alloy improves its oxidation resistance below 25 wt. %. When the

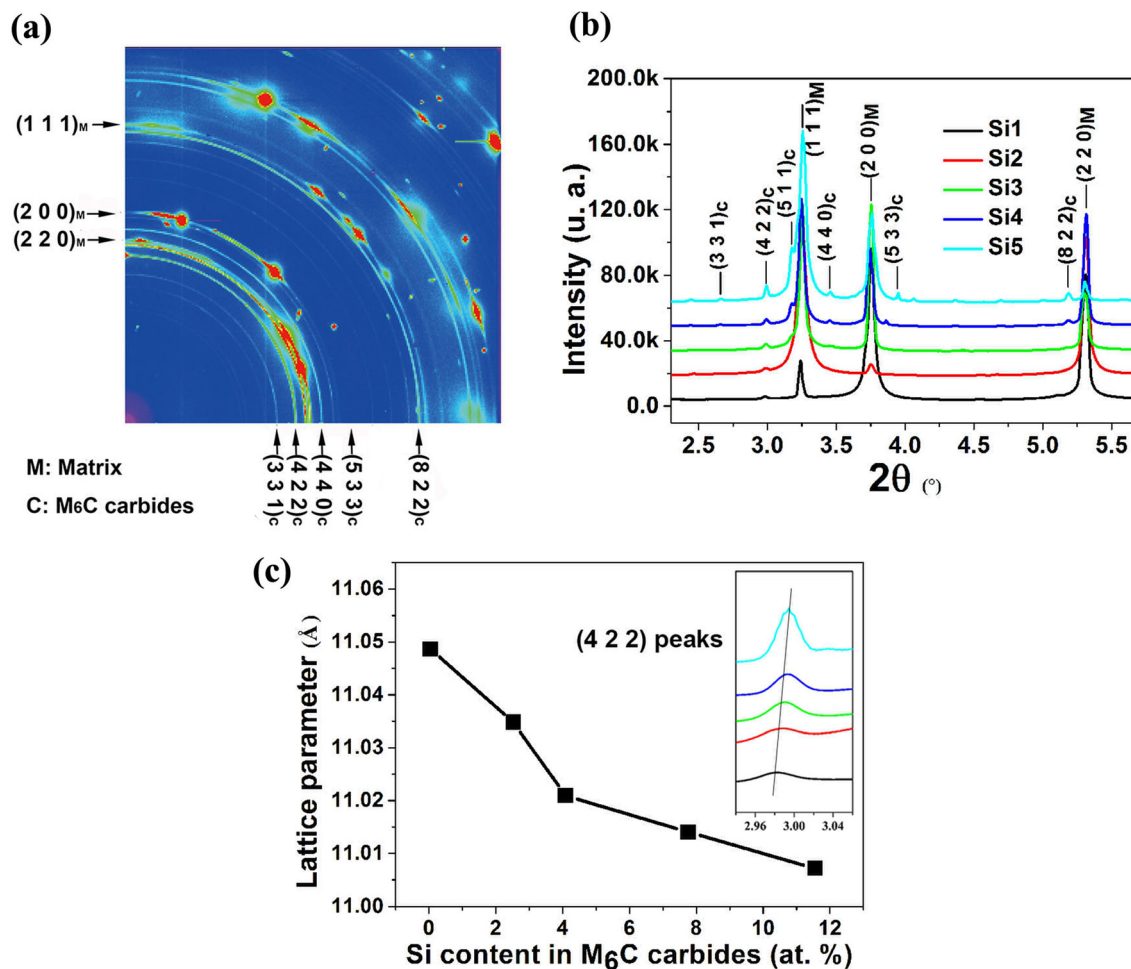
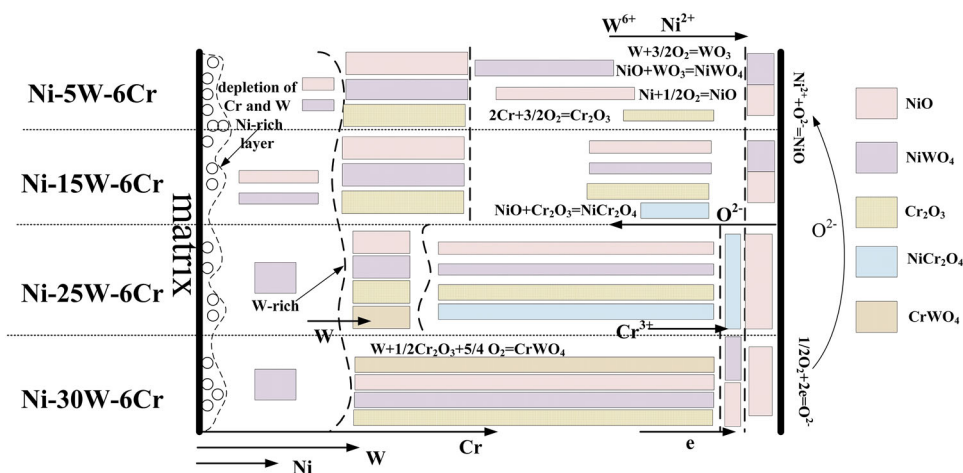


**Fig. 7** (Color online) Typical (a) 2D and (b) 1D XRD patterns for alloys with different Si concentrations. (c) Relationship between the lattice parameters and Si concentrations in  $M_6C$  carbides (reprinted from [61])

**Fig. 8** (Color online) Distribution of oxides and the related oxidation reaction in the Ni-xW-6Cr alloys



concentration of W exceeds 25 wt. %, the excessive W concentration consumes  $Cr_2O_3$  to form  $CrWO_4$  (which is also found in the oxidized Ni-25 W-6Cr alloy, as shown in Fig. 9 (h)), therefore restraining the formation of protective

$NiCr_2O_4$ . The existence of  $CrWO_4$  destroys the compactness of  $NiCr_2O_4$  and provides the breakaway throughout the scales as the diffusion paths for oxygen and metallic ions. It is clear that without the high spatial resolution of

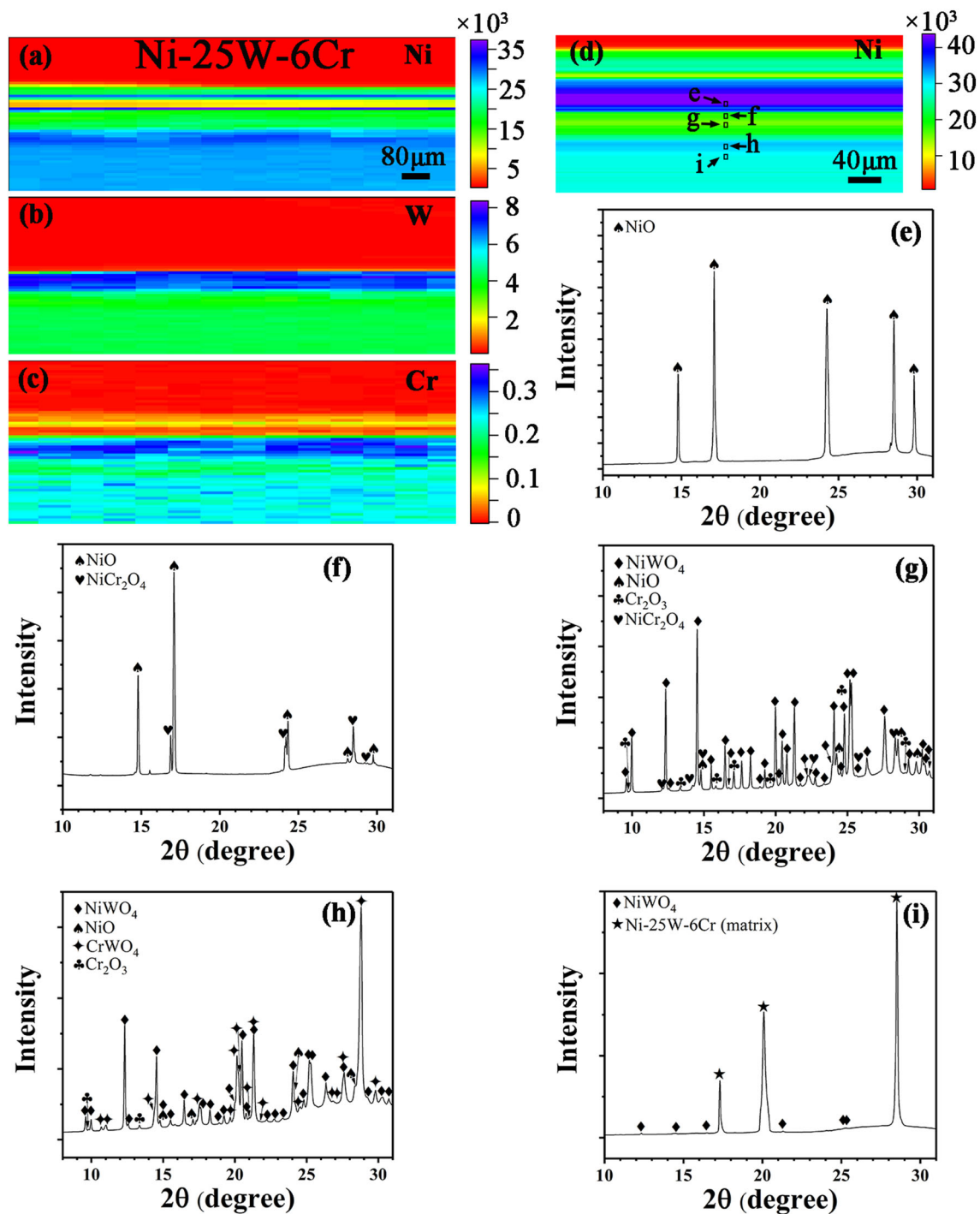


**Fig. 9** (Color online) Element mapping by  $\mu$ -XRF for (a) Ni, (b) W, and (c) Cr at low magnification and (d) for Ni at high magnification in Ni-25 W-6Cr alloy. (e-i)  $\mu$ -XRD patterns at the selected positions as

marked in Fig. 9d in the Ni-25 W-6Cr alloy TEM specimen (adapted from [36])

synchrotron radiation technologies, it is hard to determine the existence of CrWO<sub>4</sub> in the scales. Moreover, it was found that the valence state of W in the corrosion products (Fig. 10) is between 4+ and 6+ rather than the strict 6+. This indicates that the tungsten oxides in the Ni-25 W-6Cr alloy are not strict stoichiometric WO<sub>3</sub>. In fact,

it has been reported that the chemical composition of tungsten oxides ranges from WO<sub>2.72</sub> to WO<sub>2.9</sub> [74]. Such deviation from the strict valent state of the oxides may also play an important role in the diffusion process of W ions. The author suggested that the optimum W content is 25–30 wt. % from the aspect of oxidation resistance.

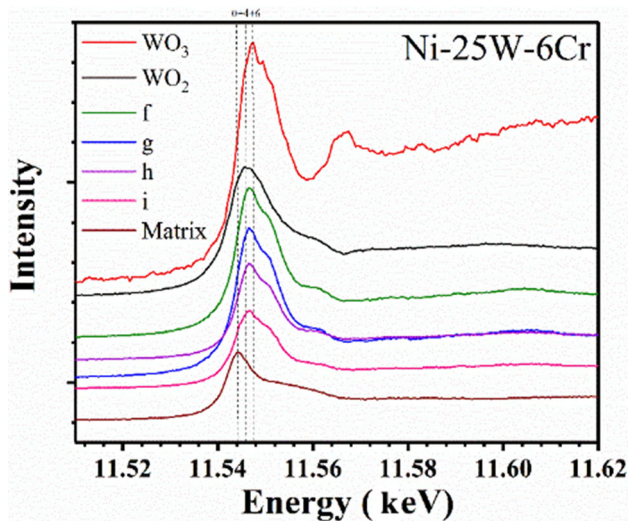


**Fig. 10** (Color online)  $\mu$ -XANES spectra for the positions marked in Fig. 9 (adapted from [36])

### 5.3 Size Distribution Study of SiC Nanoparticles in Ni-SiC by USAXS

As mentioned above, the helium embrittlement problem can be effectively reduced by the addition of Ti, Nb, Zr, and Hf, which form fine MC carbides to trap the helium atoms at their interface with the matrix and prevent the growth of helium bubbles at grain boundaries [22]. From another perspective, the direct addition of molten salt corrosion-resistant nanoparticles to the matrix could be a promising solution. Therefore, bulk Ni-SiC<sub>NP</sub> composite materials have been developed for their potential application in MSR [75]. This material exhibits stronger helium absorbing capability than pure nickel and hence mitigates helium embrittlement. The density and size distribution of the particles directly determine the capacity for helium trapping, which should be measured accurately. Xie and her co-workers carried out such measurements in a Ni-SiC<sub>NP</sub> composite by USAXS [75]. They found that SiC nanoparticles are almost evenly distributed in the pure Ni matrix. By modeling the USAXS data, the size distribution, number density, and interparticle distances of the SiC nanoparticles were obtained, which agree with those obtained from TEM (Fig. 11). The appropriate usage of USAXS in the simplified model materials reveals its potential for characterizing nanosized MC carbides in modified Hastelloy N. It has been found that the addition of different MC carbide-forming elements leads to different helium trapping capacities. USAXS could provide an interpretation for such capacities from the point of microstructures, namely the presence of MC carbides in the modified Hastelloy N alloys.

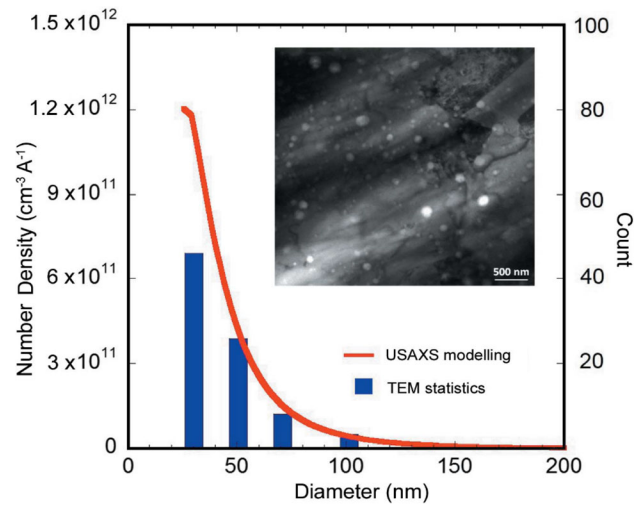


**Fig. 11** (Color online) Comparability between TEM and USAXS characterization methods for the distribution of SiC particles in the Ni-SiC sample (from [75], reproduced with permission of the International Union of Crystallography)

## 6 Summary and Perspective

Synchrotron radiation techniques have already proved to be powerful for the study of alloy materials for MSRs. The related studies have advanced the understanding of molten salt and Te corrosion from a microscopic point of view. Moreover, the applications of synchrotron radiation techniques have promoted the optimization of the GH3535 alloy with more appropriate Si content, and the design of new alloys, such as a strengthened dispersion alloy. So far, most studies based on synchrotron radiation techniques were aimed at the Hastelloy N or its improved versions, such as GH3535. New alloy materials for MSRs would receive more and more attention and would expand the application of synchrotron radiation techniques. The mechanical properties, atomic configuration, and precipitates (MC carbides or  $\gamma'$  phases), to name a few, could be investigated. The atomic configuration of these new additional elements, such as Nb, Ti, Al, and W, in the different alloys (Table 1), should be explored by XAFS to determine their strengthening mechanism. Preliminary experiments for the W atoms in a Ni-W-Cr alloy are underway. USAXS and HERXRD can help us to design the appropriate distribution and interfacial mismatch of nanosized MC carbides in the Ti-modified and Nb-modified alloys, which are related to their strengthening and helium trapping effects. The mechanism of Te corrosion resistance from Nb and Al additions is still unclear. The formation of protective layers containing Nb and Al on the surface of alloys is a possible scenario, which can be examined by STXM and XAS. Overall, synchrotron-based material characterization

techniques can shed light on alloy materials for MSRs, and more investigations should be performed.

Furthermore, the experimental capability of SSRF can be enhanced by the update of Phase-I beamlines [76–81], and the Phase-II beamline project (including sixteen new beamlines), which was officially started on 20 November 2016, with a construction period of 6 years. It is expected that the new beamlines will create opportunities for the study of MSR alloy materials. The most anticipated beamlines in the Phase-II project include the Laue microdiffraction and ultra-hard X-ray beamlines. Laue microdiffraction is a powerful characterization technique for the study of the microstructures and mechanical properties of alloys at the sub-micron level, which offers the distinct advantages of simple specimen preparation and flexible operating environment, compared with the similar electron backscatter diffraction (EBSD) technique [9]. The properties of alloy materials are expected to be measured in the simulative MSR environment (Te vapor or molten salt) by the Laue microdiffraction. In the future, the upgraded SSRF, together with the synchrotron radiation facilities in other countries and regions, is expected to promote the development of MSR alloy materials.

## References

1. L. Mathieu, D. Heuer, R. Brissot et al., The thorium molten salt reactor: Moving on from the MSBR. *Prog. Nucl. Energ.* **48**, 664 (2006). <https://doi.org/10.1016/j.pnucene.2006.07.005>
2. P.N. Haubenreich, J. Engel, Experience with the molten-salt reactor experiment. *Nucl. Technol.* **8**, 118 (1970). <https://doi.org/10.13182/NT8-2-118>
3. J. Serp, M. Allibert, O. Beneš et al., The molten salt reactor (MSR) in generation IV: Overview and perspectives. *Prog. Nucl. Energy* **77**, 308 (2014). <https://doi.org/10.1016/j.pnucene.2014.02.014>
4. H. Xu, Thorium energy and molten salt reactor R&D in China. Paper Presented at Proceedings of the ThEC13 Conference, CERN, Globe of Science and Innovation (Geneva, Switzerland, October 27–31, 2013)
5. H.E. McCoy, The INOR-8 Story. *Oak Ridge Natl. Lab. Rev.* **3**, 35 (1969)
6. H. McCoy Jr., *Status of materials development for molten salt reactors* (Oak Ridge National Lab, TN (USA), 1978)
7. Z. Li, B. Leng, G. Yuan et al., R&D of Structural alloy for molten salt reactor in China. Paper presented at ASME 2016 pressure vessels and piping conference (Vancouver, British Columbia, Canada, July 17–21, 2016)
8. G. Bruno, G. Schumacher, H.C. Pinto et al., Measurement of the lattice misfit of the nickel-base superalloy SC16 by high-energy synchrotron radiation. *Metall. Mater. Trans. A* **34**, 193 (2003). <https://doi.org/10.1007/s11661-003-0321-8>
9. G. Zhou, J. Kou, Y. Li et al., Quantitative scanning Laue diffraction microscopy: Application to the study of 3D printed nickel-based superalloys. *Quantum Beam Science* **2**, 13 (2018). <https://doi.org/10.3390/qbs2020013>
10. G. Zhou, W. Zhu, H. Shen et al., Real-time microstructure imaging by Laue microdiffraction: A sample application in laser 3D printed Ni-based superalloys. *Scientific reports* **6**, 28144 (2016). <https://doi.org/10.1038/srep28144>
11. L. Liu, N.S. Hussein, C.J. Torbet et al., In situ imaging of high cycle fatigue crack growth in single crystal nickel-base superalloys by synchrotron X-radiation. *J. Eng. Mater. Technol.* **130**, 021008 (2008). <https://doi.org/10.1115/1.2840966>
12. T. Link, S. Zabler, A. Epishin et al., Synchrotron tomography of porosity in single-crystal nickel-base superalloys. *Mater. Sci. Eng., A* **425**, 47 (2006). <https://doi.org/10.1016/j.msea.2006.03.005>
13. M. Jensen, D. Dye, K. James et al., Residual stresses in a welded superalloy disc: Characterization using synchrotron diffraction and numerical process modeling. *Metall. Mater. Trans. A* **33**, 2921 (2002). <https://doi.org/10.1007/s11661-002-0277-0>
14. X.-X. Ye, H. Ai, Z. Guo et al., The high-temperature corrosion of Hastelloy N alloy (UNS N10003) in molten fluoride salts analysed by STXM, XAS, XRD, SEM, EPMA, TEM/EDS. *Corros. Sci.* **106**, 249–259 (2016). <https://doi.org/10.1016/j.corsci.2016.02.010>
15. J. He, Z. Zhao, Shanghai synchrotron radiation facility. *National Science Review* **1**, 171 (2014). <https://doi.org/10.1093/nsr/nwt039>
16. E.C. Miller. *Metallurgy and Materials*. in: Ellis CB, Thompson WE, (Eds.). *Aircraft Nuclear Propulsion Project Quarterly Progress Report for Period Ending August 31, 1950* (ORNL-858). (Oak Ridge National Laboratory, TN (USA), 1950). pp. 61
17. W.B.e. Cottrell. *Aircraft Nuclear Propulsion Project Quarterly Progress Report for Period Ending March 10, 1952* (ORNL-1227), (Oak Ridge National Laboratory, TN (USA), 1952)
18. W.H. Jordan, S.J. Cromer, A.J. Miller, *Aircraft Nuclear Propulsion Project Quarterly Progress Report for Period Ending March 31, 1957* (ORNL-2274, parts 1-5) (Oak Ridge National Laboratory, TN (USA), 1957)
19. H.E.J. McCoy, J.R.J. Weir, *Materials Development for Molten-Salt Breeder Reactors (ORNL-TM-1854)* (Oak Ridge National Laboratory, TN (USA), 1967)
20. H.E. McCoy, B. McNabb, *Intergranular cracking of INOR-8 in the MSRE (ORNL-4829)* (Oak Ridge National Laboratory, TN (USA), 1972)
21. W.R. Martin, H.E. McCoy, J.R. Weir, *Production of a Low-Boron Heat of Hastelloy N (ORNL-TM-1146)* (Oak Ridge National Laboratory, TN (USA), 1965)
22. H. McCoy Jr., *Influence of titanium, zirconium, and hafnium additions on the resistance of modified Hastelloy N to irradiation damage at high temperature: Phase I* (Oak Ridge National Lab, TN (USA), 1971)
23. M. Hron, M. Mikisek, Experimental verification of design input of the SPHINX concept of MSR (project EROS—Experimental zero power salt reactor SR-0). *Prog. Nucl. Energ.* **50**, 230 (2008). <https://doi.org/10.1016/j.pnucene.2007.11.003>
24. V. Ignatiev, A. Surenkov, I. Gnidoj et al., Intergranular tellurium cracking of nickel-based alloys in molten Li, Be, Th. U/F salt mixture. *J Nucl Mater* **440**, 243 (2013). <https://doi.org/10.1016/j.jnucmat.2013.05.001>
25. S. Delpech, E. Merle-Lucotte, T. Auger et al., MSFR: Material issues and the effect of chemistry control. Paper Presented at Gen-IV international forum (GIF): 10 years of achievements and the path forward (Paris, France, 9–10 Sep 2009)
26. R. Wright, T. Sham, *Status of metallic structural materials for molten salt reactors* (Idaho National Lab, Idaho Falls, 2018)
27. H.J. Xu, Z.T. Zhao, Current status and progresses of SSRF project. *Nucl. Sci. Tech.* **19**, 1 (2008). [https://doi.org/10.1016/S1001-8042\(08\)60013-5](https://doi.org/10.1016/S1001-8042(08)60013-5)

28. Q.-S. Wang, Q.-Y. Pan, K. Liu et al., The macromolecular crystallography beamline of SSRF. Nucl. Sci. Tech. 26, 10102 (2015). <https://doi.org/10.13538/j.1001-8042/nst.26.010102>
29. Y. Hai-Sheng, W. Xiang-Jun, L. Jiong et al., The XAFS beamline of SSRF. Nucl. Sci. Tech. 050102 (2015). <http://dx.doi.org/10.13538/j.1001-8042/nst.26.050102>
30. Y. Tie-Ying, W. Wen, Y. Guang-Zhi et al., Introduction of the X-ray diffraction beamline of SSRF. Nucl. Sci. Tech. 26, 20101 (2015). <https://doi.org/10.13538/j.1001-8042/nst.26.020101>
31. L.-L. Zhang, S. Yan, S. Jiang et al., Hard X-ray micro-focusing beamline at SSRF. Nucl. Sci. Tech. 26, 060101 (2015). <http://dx.doi.org/10.13538/j.1001-8042/nst.26.060101>
32. H.-L. Xie, B. Deng, G.-H. Du et al., Latest advances of X-ray imaging and biomedical applications beamline at SSRF. Nucl. Sci. Tech. 26, 020102 (2015). <http://dx.doi.org/10.13538/j.1001-8042/nst.26.020102>
33. L.-J. Zhang, Z.-J. Xu, X.-Z. Zhang et al., Latest advances in soft X-ray spectromicroscopy at SSRF. Nucl. Sci. Tech. 26, 040101 (2015). <http://dx.doi.org/10.13538/j.1001-8042/nst.26.040101>
34. C. Xue, Y. Wang, Z. Guo et al., High-performance soft x-ray spectromicroscopy beamline at SSRF. Rev. Sci. Instrum. **81**, 103502 (2010). <https://doi.org/10.1063/1.3491837>
35. F. Tian, X.-H. Li, Y.-Z. Wang et al., Small angle X-ray scattering beamline at SSRF. Nucl. Sci. Tech. 26, 030101 (2015). <http://dx.doi.org/10.13538/j.1001-8042/nst.26.030101>
36. R. Gao, X.-X. Ye, S. Yan et al., Effects of tungsten content on the high-temperature oxidation behavior of Ni-xW-6Cr alloys. Corros. Sci. **149**, 87 (2019). <https://doi.org/10.1016/j.corsci.2019.01.008>
37. G. Zheng, B. Kelleher, L. He et al., High-temperature corrosion of UNS N10003 in molten Li<sub>2</sub>BeF<sub>4</sub> (FLiBe) salt. Corrosion **71**, 1257 (2015). <https://doi.org/10.5006/1657>
38. G. Zheng, B. Kelleher, G. Cao et al., Corrosion of 316 stainless steel in high temperature molten Li<sub>2</sub>BeF<sub>4</sub> (FLiBe) salt. J. Nucl. Mater. **461**, 143 (2015). <https://doi.org/10.1016/j.jnucmat.2015.03.004>
39. C. Sona, B. Gajbhiye, P. Hule et al., High temperature corrosion studies in molten salt-FLiNaK. Corros. Eng., Sci. Technol. **49**, 287 (2014). <https://doi.org/10.1179/1743278213Y.0000000135>
40. F.-Y. Ouyang, C.-H. Chang, J.-J. Kai, Long-term corrosion behaviors of Hastelloy-N and Hastelloy-B3 in moisture-containing molten FLiNaK salt environments. J. Nucl. Mater. **446**, 81 (2014). <https://doi.org/10.1016/j.jnucmat.2013.11.045>
41. F.-Y. Ouyang, C.-H. Chang, B.-C. You et al., Effect of moisture on corrosion of Ni-based alloys in molten alkali fluoride FLiNaK salt environments. J. Nucl. Mater. **437**, 201 (2013). <https://doi.org/10.1016/j.jnucmat.2013.02.021>
42. L. Olson. Material corrosion in molten LiF-NaF-KF eutectic salt. University of Wisconsin-Madison, PhD Dissertation, 2009
43. D.F. Williams, L.M. Toth, K.T. Clarno, *Assessment of candidate molten salt coolants for the advanced high temperature reactor (AHTR)* (Department of Energy, United States, 2006)
44. N.S. Patel, V. Pavlík, M. Boča, High-temperature corrosion behavior of superalloys in molten salts – A review. Crit. Rev. Solid State Mater. Sci. **42**, 83 (2016). <https://doi.org/10.1080/10408436.2016.1243090>
45. K. Sridharan, T.R. Allen. 12 - Corrosion in Molten Salts. in: Groult FL, (Ed.). Molten Salts Chemistry. (Elsevier, Oxford, 2013). pp. 241
46. T. Bauer, N. Pfeleger, D. Laing et al. 20 - High-Temperature Molten Salts for Solar Power Application. in: Groult FL, (Ed.). Molten Salts Chemistry. (Elsevier, Oxford, 2013). pp. 415
47. W. Ding, A. Bonk, T. Bauer, Corrosion behavior of metallic alloys in molten chloride salts for thermal energy storage in concentrated solar power plants: A review. Frontiers of Chemical Science and Engineering **12**(3), 564 (2018). <https://doi.org/10.1007/s11705-018-1720-0>
48. P. Calderoni, C. Cabet. 23 - Corrosion issues in molten salt reactor (MSR) systems. in: Féron D, (Ed.). Nuclear Corrosion Science and Engineering. (Woodhead Publishing, 2012). pp. 842
49. J.R. Keiser. Compatibility Studies of Potential Molten-Salt Breeder Reactor Materials in Molten Fluoride Salts, (Oak Ridge National Laboratory, 1977)
50. J.W. Koger, Fluoride salt corrosion and mass transfer in high temperature dynamic systems. Corrosion **29**, 115 (1973). <https://doi.org/10.5006/0010-9312-29.3.115>
51. Y. Wang, H. Liu, C. Zeng, Galvanic corrosion of pure metals in molten fluorides. J. Fluor. Chem. **165**, 1 (2014). <https://doi.org/10.1016/j.jfluchem.2014.05.010>
52. L.C. Olson, J.W. Ambrosek, K. Sridharan et al., Materials corrosion in molten LiF-NaF-KF salt. J. Fluorine Chem. **130**, 67 (2009). <https://doi.org/10.1016/j.jfluchem.2008.05.008>
53. M. Liu, J. Zheng, Y. Lu et al., Investigation on corrosion behavior of Ni-based alloys in molten fluoride salt using synchrotron radiation techniques. J. Nucl. Mater. **440**, 124 (2013). <https://doi.org/10.1016/j.jnucmat.2013.04.056>
54. D. Olander, Redox condition in molten fluoride salts - Definition and control. J. Nucl. Mater. **300**, 270 (2002). [https://doi.org/10.1016/0022-3115\(01\)00742-5](https://doi.org/10.1016/0022-3115(01)00742-5)
55. D. Ingersoll, C. Forsberg, P. MacDonald, Trade Studies on the Liquid-Salt-Cooled Very High-Temperature Reactor: Fiscal Year 2006 Progress Report. ORNL/TM-2006/140, Oak Ridge National Laboratory (2007)
56. Y. Jia, H. Cheng, J. Qiu et al., Effect of temperature on diffusion behavior of Te into nickel. J. Nucl. Mater. **441**, 372 (2013). <https://doi.org/10.1016/j.jnucmat.2013.06.025>
57. L. Jiang, C.-T. Fu, B. Leng et al., Influence of grain size on tellurium corrosion behaviors of GH3535 alloy. Corros. Sci. **148**, 110 (2019). <https://doi.org/10.1016/j.corsci.2018.12.007>
58. L. Lu, Y. Jia, X.-X. Ye et al., Local structure study of tellurium corrosion of nickel alloy by X-ray absorption spectroscopy. Corros. Sci. **108**, 169 (2016). <https://doi.org/10.1016/j.corsci.2016.03.006>
59. M. Luo, L. Li, F. Song et al., XAFS and SRGI-XRD studies of the local structure of tellurium corrosion of Ni-18%Cr alloy. Nucl. Sci. Tech. **30**, 153 (2019). <https://doi.org/10.1007/s41365-019-0673-4>
60. Z.-F. Xu, J.-S. Dong, L. Jiang et al., Effects of Si Addition and Long-Term Thermal Exposure on the Tensile Properties of a Ni-Mo-Cr Superalloy. Acta Metallurgica Sinica (English Letters) **28**, 951 (2015). <https://doi.org/10.1007/s40195-015-0277-x>
61. L. Jiang, X.-X. Ye, Z.-Q. Wang et al., The critical role of Si doping in enhancing the stability of M<sub>6</sub>C carbides. J Alloys Compd **728**, 917 (2017). <https://doi.org/10.1016/j.jallcom.2017.09.042>
62. K. Kuo, The formation of η carbides. Acta Metall. **1**, 301 (1953). [https://doi.org/10.1016/0001-6160\(53\)90103-5](https://doi.org/10.1016/0001-6160(53)90103-5)
63. K. Frisk, J. Bratberg, A. Markström, Thermodynamic modelling of the M<sub>6</sub>C carbide in cemented carbides and high-speed steel. Calphad. **29**, 91 (2005). <https://doi.org/10.1016/j.calphad.2005.07.001>
64. Q. Wu, H. Song, R.W. Swindeman et al., Microstructure of long-term aged IN617 Ni-base superalloy. Metall. Mater. Trans. A **39**, 2569 (2008). <https://doi.org/10.1007/s11661-008-9618-y>
65. H. Wisell, An experimental study of carbide/austenite equilibria in the high-speed steel alloy system. Metall. Trans. A **22**, 1391 (1991). <https://doi.org/10.1007/BF02660671>
66. L. Dobrzański, The structure and properties of WV high-speed steels with increased content of silicon. J. Mater. Process. Tech **56**, 933 (1996). [https://doi.org/10.1016/0924-0136\(96\)85121-1](https://doi.org/10.1016/0924-0136(96)85121-1)

67. S. Liu, X.-X. Ye, L. Jiang et al., Effect of tungsten content on the microstructure and tensile properties of Ni-xW-6Cr alloys. *Mater. Sci. Eng., A* **655**, 269 (2016). <https://doi.org/10.1016/j.msea.2016.01.010>
68. H. Ai, X.-X. Ye, L. Jiang et al., On the possibility of severe corrosion of a Ni-W-Cr alloy in fluoride molten salts at high temperature. *Corros. Sci.* **149**, 218 (2019). <https://doi.org/10.1016/j.corsci.2019.01.012>
69. S. Fabre, J. Finne, P. Chamelot et al., Corrosion of metallic materials for molten salt reactors. Paper Presented at Proceedings of ICAPP'09 (Tokyo, Japan)
70. S. Espevik, R.A. Rapp, P.L. Daniel et al., Oxidation of Ni-Cr-W ternary alloys. *Oxid. Met.* **14**, 85 (1980). <https://doi.org/10.1007/bf00603987>
71. D.B. Lee, J.H. Ko, S.C. Kwon, Oxidation of Ni-W coatings at 700 and 800 °C in air. *Surf. Coat. Technol.* **193**, 292 (2005). <https://doi.org/10.1016/j.surfcoat.2004.08.151>
72. S.-J. Park, S.-M. Seo, Y.-S. Yoo et al., Statistical Study of the Effects of the Composition on the Oxidation Resistance of Ni-Based Superalloys. *J Nanomater* **2015**, 1 (2015). <https://doi.org/10.1155/2015/929546>
73. X.X. Huang, J.S. Li, R. Hu et al., Evolution of oxidation in Ni-Cr-W alloy at 1100 °C. *Rare Metal Mat. Eng.* **39**, 1908 (2010). [https://doi.org/10.1016/s1875-5372\(10\)60136-1](https://doi.org/10.1016/s1875-5372(10)60136-1)
74. K.T. Jacob, Phase relationships in the system Cr-W-O and thermodynamic properties of CrWO<sub>4</sub> and Cr<sub>2</sub>WO<sub>6</sub>. *Journal of Materials Science* **15**, 2167 (1980). <https://doi.org/10.1007/bf00552303>
75. R. Xie, J. Ilavsky, H. Huang et al., Dispersed SiC nanoparticles in Ni observed by ultra-small-angle X-ray scattering. *J. Appl. Crystallogr.* **49**, 2155 (2016). <https://doi.org/10.13538/j.1001-8042/nst.26.020102>
76. X. Sun, W. Zhu, Z. Xu et al., Design of a cryo-cooled double multilayer monochromator in USAXS beamline at SSRF. *Nucl. Tech.* **42**, 110101 (2019). <https://doi.org/10.11889/j.0253-3219.2019.hjs.42.110101> (in Chinese)
77. B. Gao, Y. Leng, H. Chen et al., Slit separation rapid scanning system for synchrotron radiation interferometer. *Nucl. Tech.* **41**, 080101 (2018). <https://doi.org/10.11889/j.0253-3219.2018.hjs.41.080101> (in Chinese)
78. Z. Zhao, H. Xu, P. Gong et al., Management and query system for the beamline operation data based on Archiver Appliance at SSRF. *Nucl. Tech.* **41**, 030102 (2018). <https://doi.org/10.11889/j.0253-3219.2018.hjs.41.030102> (in Chinese)
79. C. Hong, C. Yang, P. Zhou et al., Study on X-ray beam stabilization of BL16B1 at SSRF. *Nucl. Tech.* **41**, 120101 (2018). <https://doi.org/10.11889/j.0253-3219.2018.hjs.41.120101> (in Chinese)
80. C. Qin, S. Xue, N. Wang et al., The finite element analysis of the bent elliptical cylindrical mirror. *Nucl. Tech.* **41**, 010101 (2018). <https://doi.org/10.11889/j.0253-3219.2018.hjs.41.010101> (in Chinese)
81. Y. Pan, C. Mao, D. Shu et al., Simulation and analysis of a high-stability flexure bending mechanism for hard X-ray submicron focusing. *Nucl. Tech.* **40**, 090102 (2017). <https://doi.org/10.11889/j.0253-3219.2017.hjs.40.090102> (in Chinese)